Enhancing AA7075 Spot Welding with Multipulsed Current and Magnetic Fields: Part 2 — Mechanical Performance

Optimizing welding parameters for defect-free aluminum joints by evaluating the effects of expulsion on weld quality and mechanical performance

BY Z. LI, Z. TENG, C. QIAN, R. CHEN, J. QUEVAL, J. BROWN, Y. XIA, AND Y. LI

Abstract

AA7075, widely used in aviation structures due to its high strength and corrosion resistance, has emerged as a promising lightweight material for automotive body applications. This study investigates the resistance spot welding (RSW) process of AA7075. Although RSW offers cost reduction and efficiency advantages, welding AA7075 presents challenges such as high thermal cracking sensitivity and severe expulsion. In Part 1, the MPMA-RSW process was introduced, which combines multipulse (MP) and magnetic-assisted (MA) techniques to address these challenges. The microstructure of the welds was systematically characterized and analyzed in detail. Part 2 focuses on analyzing the mechanical properties and expulsion behavior of AA7075 RSW joints, including tensile-shear strength and fracture morphology. By evaluating the effects of expulsion on weld quality and mechanical performance, this research aims to provide insights for optimizing welding parameters to produce defect-free, high-quality aluminum joints. Additionally, it contributes to advancing AA7075 applications in critical industries by improving the weldability and mechanical properties of RSW joints.

https://doi.org/10.29391/2025.104.033

Keywords

- AA7075
- Resistance Spot Welding
- Magnetically Assisted
- Multipulse Current
- Fracture Mode
- Expulsion Behavior

Introduction

Known for its high mechanical strength and resistance to corrosion, AA7075 was initially used in aviation and is now progressively being integrated into the body structures of automobiles and high-speed trains (Ref. 1). Utilizing resistance spot welding (RSW), a process commonly employed in those industries, for joining AA7075 materials can allow for maintaining cost efficiency, thanks to the low cost and reliability of the process, while minimizing assembly line changes. However, the high solidification cracking sensitivity and severe expulsion occurring during welding pose challenges to the use of the RSW process (Ref. 2). To address these issues, the MPMA-RSW process was proposed in Part 1 of this paper, and the nugget morphology and microstructure under different process combinations were investigated (Ref. 3). This process combines the multipulse (MP) with magnetically assisted (MA) techniques to achieve RSW joints without significant defects. Part 2 systematically investigates the expulsion behavior, mechanical properties, and fracture morphology of welded joints under different processing combinations.

Welding expulsion significantly impacts the quality of spot welds. Generally, expulsion increases the indentation of the nugget and decreases the nugget diameter and mechanical performance (Ref. 4). The mechanism and the prediction models of expulsion were deeply studied. Zhang presented a force balance model, showing that expulsion happens when the nugget pressure exceeds the electrode pressure (Refs. 5, 6). Valaee-Tale et al. modified this model and considered the effects of mechanical properties (especially yield strength) of worksheets, the diameter of electrode tips, the yield stress, and the thickness of the sheets (Ref. 7). Measuring expulsion through the RSW process signals has become a mainstream method. C. Ma et al. observed that when expulsion occurs, signals such as dynamic resistance, electrode force, and displacement all exhibit a sharp decline (Ref. 8). Among these signals, the force signal is a highly sensitive, non-susceptible method (Ref. 9) and is the most suitable method to detect expulsion occurrence. Xia et al. proposed a method for predicting expulsion by the sudden change of the force signal (Refs. 10, 11). Recent advancements in multiphysical process simulations, such as those by Lv et al. (Ref. 12), enabled the generation of synthetic data to validate expulsion detection models and optimize signal-based monitoring techniques, offering a deeper understanding of dynamic signals during welding.

Researchers often assess the quality of spot welds through tensile-shear tests. Typically, tensile-shear fractures can be classified into interfacial fractures (IFs), partial thickness fractures (PTFs), partial button fractures (PBFs), and button fractures (BFs). Achieving high-toughness BFs is considered a hallmark of high-performance weld spots (Ref. 13). P. Wung et al. studied rotation during the tensile-shear process and established failure rules, including the contributions of tensile shear and peel bending (Ref. 14). Chao established a tensile-shear performance prediction model that considered the rotation of the workpiece and failure theory during the tensile-shear process (Ref. 15). M. Pouranvari et al. proposed a model to determine the critical nugget diameter for the transition from the IF fracture mode induced by shear stress to the BF fracture mode induced by tensile stress (Ref. 16). Chen et al. established a model to estimate the critical nugget diameter of the fracture mode transition by analyzing the stress field of the heat-affected zone (Ref. 17). The above models show that the main factors affecting the mechanical properties of tensile-shear tests are nugget diameter, defects (Ref. 18), the hardness of different zones of the weld, the degree of rotation, or the thickness of the sheet.

Another difficulty with the RSW Al-Al process is obtaining a BF mode when welding thick aluminum sheets. R.S. Florea studied the tensile-shear tests of 2-mm-thick AA6061 RSW using different parameters; all of the results showed interfacial fracture (Ref. 19). Huang et al. applied the MA process to the RSW of 3-mm-thick AA6061, and the fracture mode transferred to PTFs of MA-RSW from IFs of traditional RSW (Ref. 20). The PTF mode means that the crack does not extend directly along the faying surface but extends inside the nugget, resulting in a longer fracture path with higher toughness and fracture energy absorption. This phenomenon also appears in the MA-RSW of 4-mm-thick A7N01 aluminum alloy (Ref. 2) and 1.6-mm-thick SiCp/2024Al composite (Ref. 21).

While prior studies have demonstrated the efficacy of MA-RSW and MP-RSW in enhancing welding quality, combining these two approaches into a composite MPMA-RSW process holds the promise of further advancing the properties of AA7075 welds. Part 2 of the study aimed to quantify the improvement in mechanical properties, including tensile strength and ductility, achieved through the MPMA-RSW process. A complete analysis of the mechanical properties will evaluate the effectiveness of the MPMA-RSW process in resolving the weldability problems of AA7075. Moreover, the insights gained from this study will facilitate the development of optimal welding parameters for producing high-quality, defect-free aluminum alloy joints with superior mechanical performances, thereby advancing the application potential of AA7075 in demanding industries.

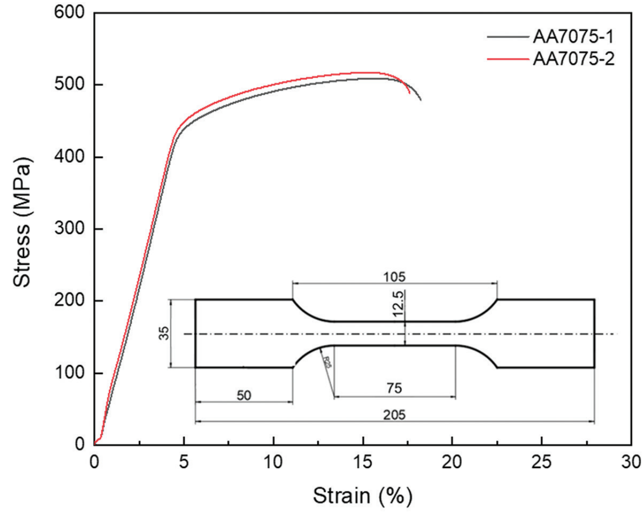

Fig. 1 — Stress-strain tensile curve and sample of AA7075 base metal (units: mm).

Table 1 — Mechanical Properties of AA7075

Yield Strength (MPa)	Ultimate Strength (MPa)	Elongation (%)
488	517	11

Experimental Procedures

Material and Testing Setup

The study utilized 2.8-mm-thick hot-stamped 7075 aluminum alloy. The mechanical properties of the base metal were tested by quasi-static tensile testing following ISO standards (Ref. 22), and the tests were conducted twice. A Zwick Z100 tensile testing machine was used. The strain rate was set at 0.002/s, and the extensometer's gauge length was 75 mm. The curves are presented in Fig. 1, and the results are shown in Table 1.

The lap-shear testing specimen is illustrated in Fig. 2. All experimental workpieces were manufactured with dimensions of 150 × 50 mm and underwent alcohol cleaning before welding. The overlap width between the two sheets was 50 mm. Additionally, 2.8-mm-thick gaskets were introduced in the clamped area during the tensile tests. Three samples for

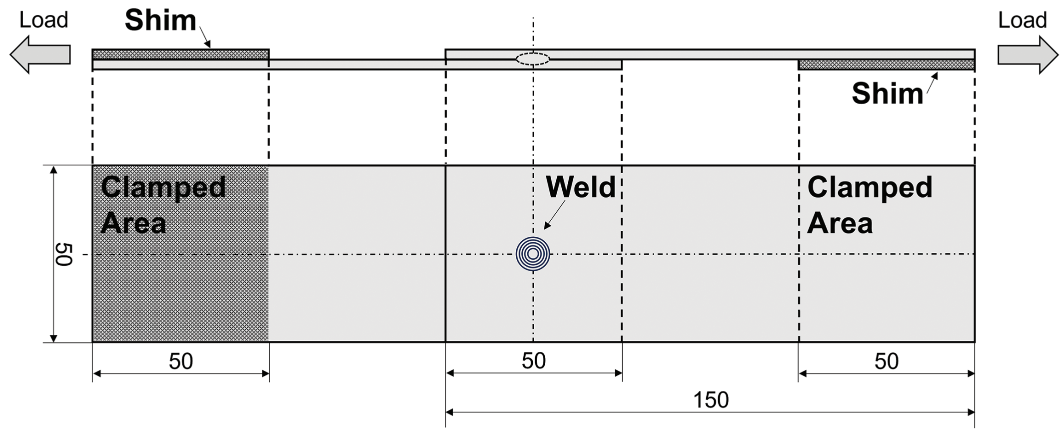

Fig. 2 — Schematic diagram of tensile-shear testing incorporated samples. Note that the tensile shear testing incorporated shims in the clamping areas (units: mm).

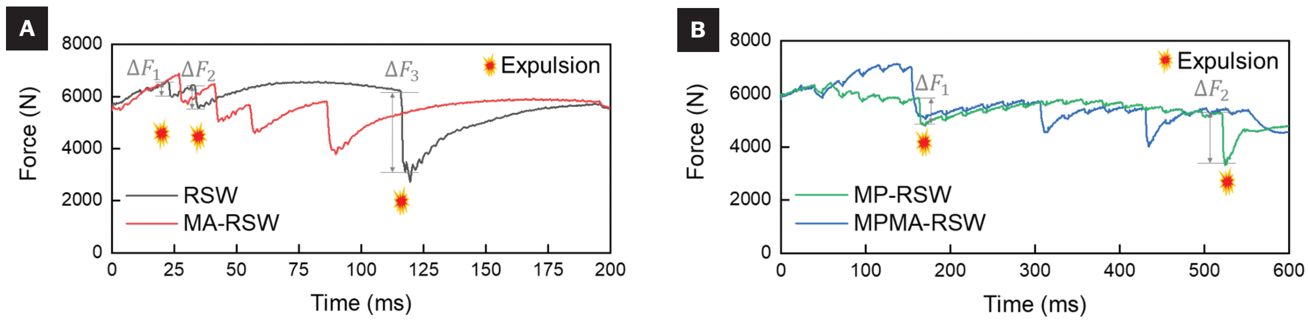

Fig. 3 — The electrode force signal curves for different welding processes: A — RSW and MA-RSW; B — MP-RSW and MPMA-RSW.

each process combination were made to ensure repeatability. Quasi-static lap-shear tests were conducted on a SUNS UTM5504 testing machine at a fixed tensile rate of 1 mm/min, and the grip-to-grip distance was 150 mm.

Welding Process

The welding process details are described in Part 1 of this paper (Ref. 3). The MFDC controller and multiring domed electrodes were used. Four different process combinations were employed, namely RSW, utilizing single-pulse parameters without the magnetically assisted (MA) method; MA-RSW, using single-pulse parameters with the MA method; MP-RSW, employing multipulse (MP) parameters without the MA method; and MPMA-RSW, utilizing the MP and MA methods together. The single and MP parameters were designed to achieve similar nugget diameters for reasonable comparisons.

Force Signal Measurement

Similar to the approach adopted in Ref. 10, an indirect measurement of the electrode force *F* was conducted using a Kistler surface strain sensor mounted on the fixed electrode arm, converting force-related surface strain into a voltage signal with 2% precision. Sensor installations were kept away from electrodes to avoid process interference. A four-channel isolated data acquisition device sampled sensor signals at 500 kSPS (samples per second) with 12-bit ENOB. Sampling values were averaged every 0.25 ms for noise reduction, and the processed data were transmitted to a personal computer via fast Ethernet in real time.

Characterization

Microhardness contours were measured using a VH1102 Vickers hardness tester. Longitudinal sections of the fractures were prepared by cutting the tested samples along their centerlines followed by polishing and etching, as described in Part 1. Longitudinal fracture photographs were then acquired using the integrated microscope of the VH1102 Vickers hardness tester. The surface morphology of the fractured welds was characterized via a VK-X260K laser scanning confocal microscope (LSCM). The projection area toward the faying surface (i.e., the 2D projection area) and the real 3D fracture surface area were measured from LSCM results. The fracture surface was observed in the secondary electron mode using a TESCAN VEGA3 scanning electron microscope.

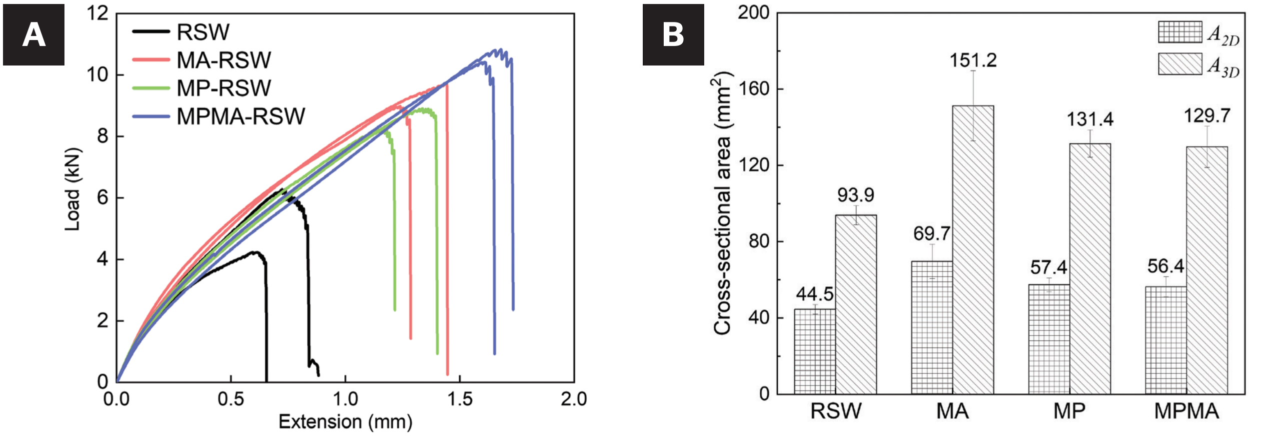

Fig. 4 — A — Load vs. extension curves of tensile-shear tests; B — the values of the fracture cross-sectional area.

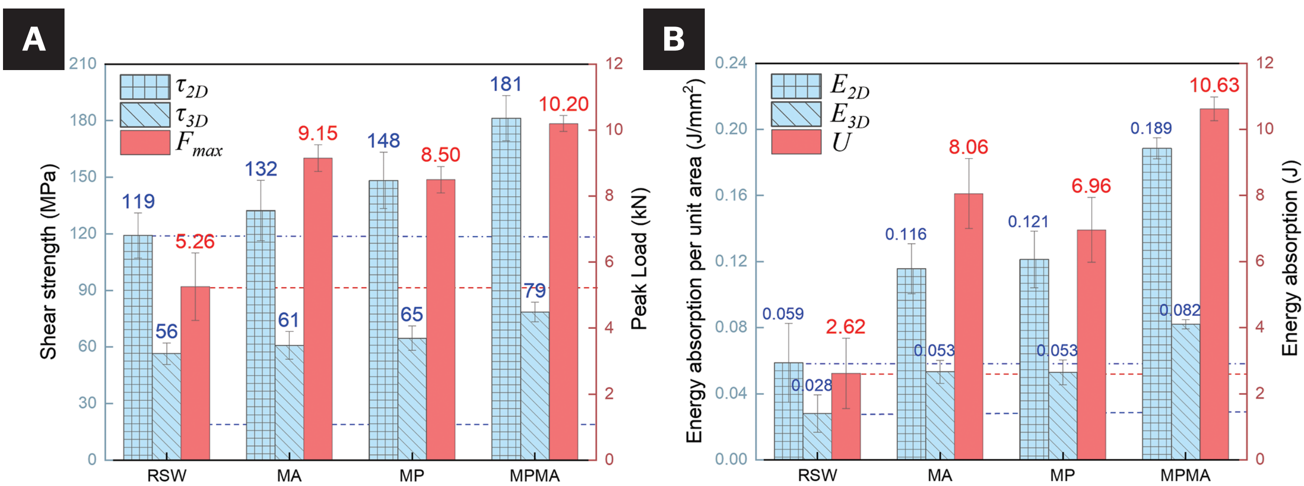

Fig. 5 — Comparison of: A — Peak load; B — energy absorption among RSW, MA-RSW, MP-RSW, and MPMA-RSW.

Results

Expulsion

The electrode force signals during the four processes are depicted in Fig. 3. The corresponding force drop, ΔF_i, is marked on the curves of RSW in Fig. 3A and MP-RSW in Fig. 3B. Each sudden drop ΔF_i in the signal represents the occurrence of expulsion. Recent control strategies (Ref. 23) have utilized such force-drop patterns to trigger real-time parameter modulation, mitigating expulsion severity. The variable *i* denotes the sequential number corresponding to the *i*th instance of force reduction during the welding process. The total electrode force drop, ΔF, was calculated by the following equation:

$$\Delta F = \sum \Delta F_i \tag{1}$$

The results showed that using single-pulse welding parameters resulted in higher frequency and amplitude of force drops than multipulse welding parameters. The stiffness of the welding gun (K_g) used in this study was measured according to (Ref. 24) and was defined as $K_g = 2896$ N/mm. The electrode displacement ΔS could be obtained from the following equation:

$$\Delta S = \frac{\Delta F}{K_g} \tag{2}$$

Since ΔS is directly proportional to the expulsion mass ΔM, the sudden drop in the electrode force signal ΔF is also directly proportional to ΔM (Ref. 10). The average measured values of ΔF for three repeats of RSW, MA, MP, and MPMA were 4350 $\pm$ 351N, 5196 $\pm$ 400N, 3016 $\pm$ 462N, and 4194 $\pm$ 426N, respectively. It can be observed that compared with RSW, MA-RSW increased the ΔM by 19.4%. Compared with MP-RSW, MPMA-RSW increased the ΔM by 39.1%.

Mechanical Performance

Figure 4A represents the curves obtained during shear tensile tests and summarizes the load and shear stress at rupture. Figure 5 shows the lap-shear performance for four processes.

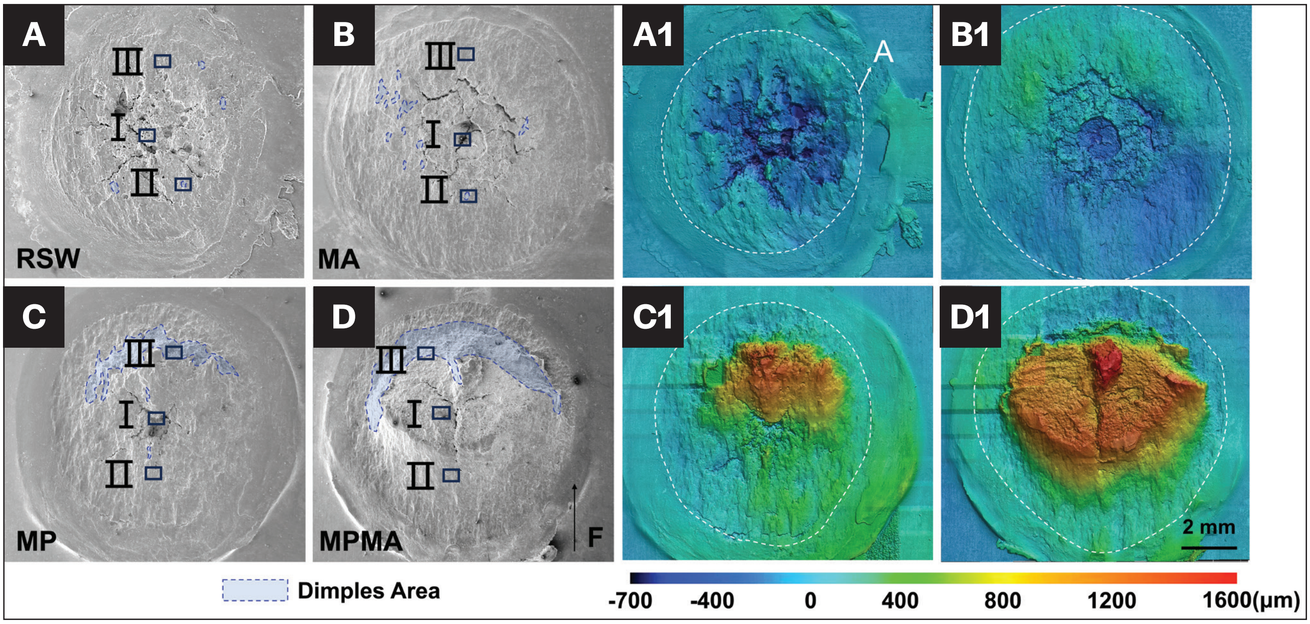

Fig. 6 — Fracture surfaces of: A — RSW; B — MA-RSW; C — MP-RSW; D — MPMA-RSW observed by SEM, and height distribution of A1 — RSW, B1 — MA-RSW, C1 — MP-RSW, and D1 — MPMA-RSW observed by LSCM. The boxes in A–D represent the positions for subsequent magnified observation, and the white dotted frames in A1–D1 outline the calculation range of the 2D fracture cross-sectional area.

It can be observed that after applying an external magnetic field, the peak load of tensile shear of MA-RSW was significantly increased by 73.5% compared with that of RSW, and the peak load of tensile shear of MPMA-RSW was increased by 20% compared with that of MP-RSW. The nugget sizes differed between the four processes, so directly comparing their mechanical performance is not necessarily simple. The cross-sectional area of the fracture surfaces, as the white dotted areas shown in Figs. 6A1-D1, was measured in Fig. 4B. To eliminate the influence of the nugget size, the projection area toward the faying surface (i.e., the 2D projection area, A_{2D}) was measured, while to eliminate the influence of different fracture modes, the real 3D fracture surface area A_{3D} was also measured. In this study, the concepts of shear strength and unit-area energy absorption were introduced, calculated as the peak force (F_{MAX}) and energy absorption (U) divided by the cross-sectional area A_{2D} and A_{3D} measured in Fig. 4B, i.e.,

$$\begin{cases} \tau_{2D} = \dfrac{F_{max}}{A_{2D}} \\ \tau_{3D} = \dfrac{F_{max}}{A_{3D}} \end{cases} \quad (3)$$

$$\begin{cases} E_{2D} = \dfrac{U}{A_{2D}} \\ E_{3D} = \dfrac{U}{A_{3D}} \end{cases} \quad (4)$$

where τ_{2D} and τ_{3D} denote the shear strength values calculated using A_{2D} and A_{3D}, respectively, whereas E_{2D} and E_{3D} represent the unit-area energy absorption values derived from A_{2D} and A_{3D}. The τ_{2D}, τ_{3D} and E_{2D}, E_{3D} for the four processes were ranked as follows: MPMA-RSW > MP-RSW ≥ MA-RSW > RSW. Compared with traditional RSW, MPMA-RSW demonstrated remarkable improvements in performance. It boosted τ_{2D} by 52.1% and enhanced E_{2D} by a substantial 220.3%. Moreover, it also increased τ_{3D} by 39.3% and raised E_{3D} by 193.6%.

Fracture Path

In Fig. 6, the RSW and MA-RSW welds show IF mode, while MP-RSW and MPMA-RSW show PTF mode after tensile-shear tests. Notably, MPMA-RSW demonstrates a significantly longer crack propagation path than MP-RSW, which can be attributed to the higher fracture scan height of MPMA-RSW compared to MP-RSW. From the surface height scan image in Figs. 6A1-D1, it is observable that RSW contains numerous defects, including pores and cracks, forming dark blue regions demonstrating a significantly lower height in the nugget center. MA-RSW exhibits a larger diameter but still follows an IF mode, with continuous cracks and pores present in the nugget center. MP-RSW has a tendency for PTFs but still shows cracks in the nugget center. MPMA-RSW demonstrates PTFs, although small cracks are still present on the button, as shown in Fig. 6D1. It is worth mentioning that when MP-RSW and MPMA-RSW were used, the cracks decreased and the void defects almost completely disappeared.

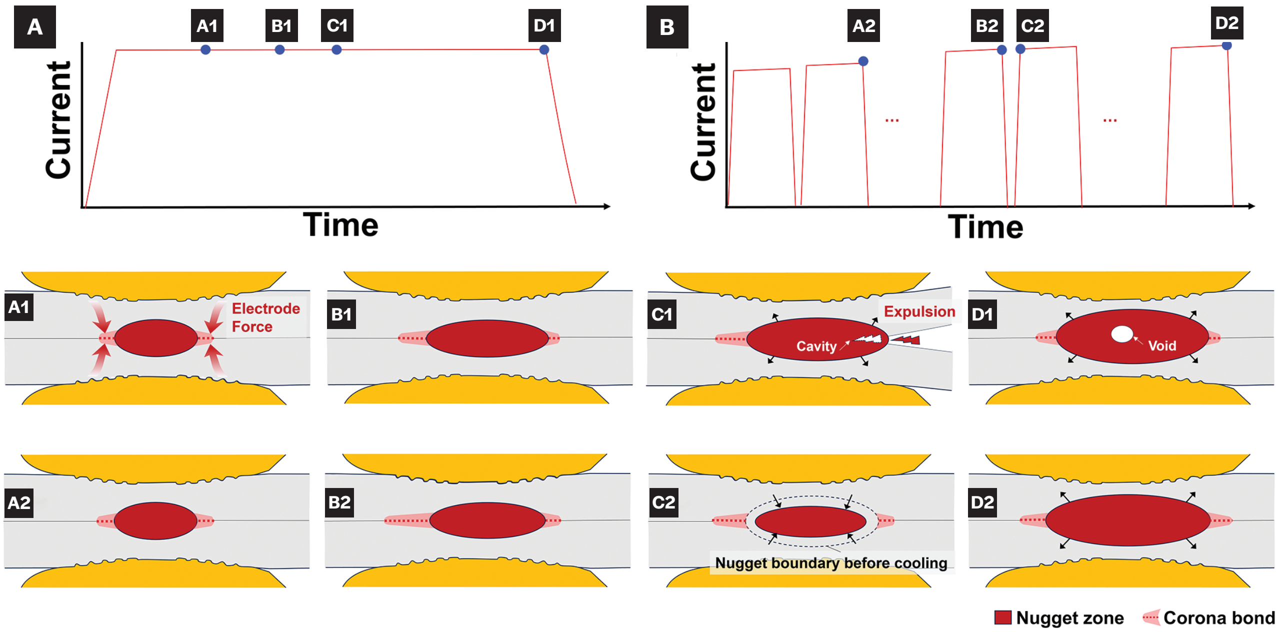

Fig. 7 — The process mechanism diagram of reducing expulsion with multipulse parameters: A — Single-stage parameters; B — MP parameters A1–D1. Schematic diagram corresponding to points A, B, C, and D in A during single-stage parameter welding (A2–D2). Schematic diagram corresponding to points A, B, C, and D in B during MP parameter welding.

Discussion

Mechanism of Expulsion

Figure 7 illustrates the mechanism by which using MP parameters suppressed expulsion. Regarding the generation of expulsion, the classical explanation posits that expulsion arises when the nugget expands at a faster rate than the corona bond expands (Ref. 4). Recent studies suggest that expulsion occurs when the stress at the sheet interface exceeds the yield stress of the high-temperature corona bond; this also means that the weld nugget lacks the plastic constraint from the surrounding area (Ref. 7). Therefore, the concept of the corona bond is still used to explain the mechanism. In the early stages of welding, the nugget and corona bond grow together, preventing the nugget from breaking through the corona bond area. In the middle stages of welding, the excessively high thermal input of single-stage parameters and nugget offset causes the nugget to break through the corona bond, resulting in expulsion and the formation of voids that eventually form porosity defects in the nugget after solidification. However, the use of MP parameters allows the nugget to cool between pulses, while the corona bond continues to grow due to the diffusion of thermal energy into the sheets, increasing the distance between the nugget and corona bond edges and, thus, limiting the risk of expulsion and the formation of porosities in the nugget.

Mechanism of Crack Propagation

To observe the crack propagation path during shear fracture, cross-sectional views of the shear fracture surfaces were extracted, as depicted in Fig. 8. Notably, cracks in both RSW and MA-RSW propagated along the interface, apparently linking with the solidification cracks during propagation. However, with the adoption of multipulse parameters, cracks in MP-RSW no longer propagated linearly between solidification cracks. The fracture paths deviated and propagated through the thickness of the nugget. As shown in Fig. 8C, the fracture path connected the void defects in the nugget center of MP-RSW, which may have been the main factor governing the propagation of cracks from the boundary to the interior of the sheet. The fracture paths in MPMA-RSW exhibited more significant deviation, bypassing the nugget center and propagating along the nugget edge. This occurrence can be attributed to the presence of internal cracks traversing the RSW and MA-RSW nuggets and the void defects concentrated at the faying surface, which served as focal points for internal crack propagation during the shear testing process. In contrast, MP-RSW and MPMA-RSW exhibited fewer defects in the center of the nugget, allowing cracks to propagate outside the faying surface plane. Although MP-RSW and MPMA-RSW exhibited PTF mode, the 3D fracture surface area, as shown in Fig. 4B, did not increase significantly compared with that of RSW and MA-RSW because the profile of each fracture surface was irregular, and cracks, pores, etc., could also have contributed to enlarging the 3D area.

Studies show that crack propagation can be influenced by hardness distribution (Ref. 2). The hardness distribution for the four processes studied is illustrated in Fig. 9. For RSW, the hardness was generally uniform, except in the void regions.

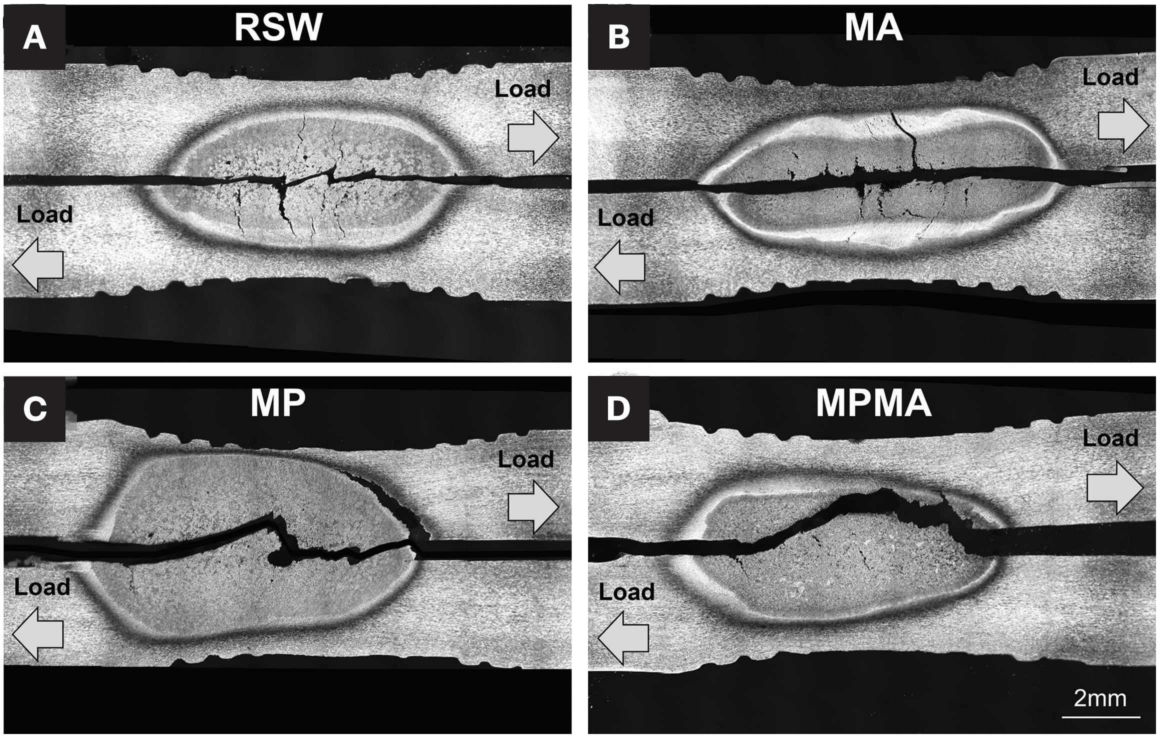

Fig. 8 — Crack path within fractured tensile-shear specimens: A — RSW; B — MA-RSW; C — MP-RSW; D — MPMA-RSW.

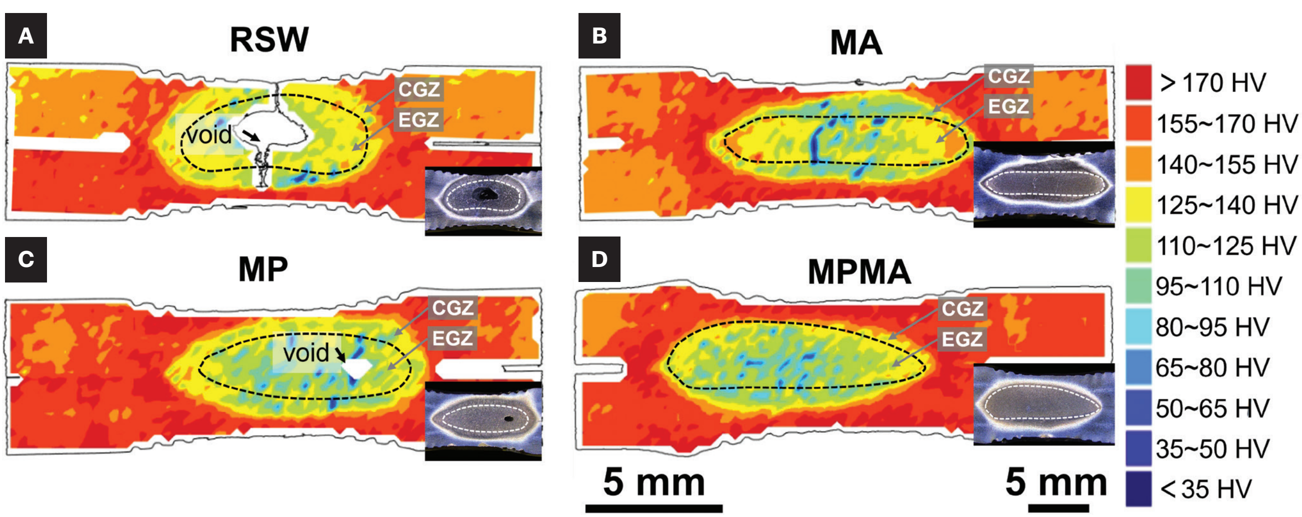

Fig. 9 — Microhardness distribution of: A — RSW; B — MA-RSW; C — MP-RSW; D — MPMA-RSW. The dashed lines are the boundaries between CGZ and EGZ.

Generally, the hardness of the columnar grain zone was lower than that of the equiaxial grain zone of the MA-RSW nugget, and such a hardness distribution showed distinct stratification. The hardness of the equiaxial grain zone was uneven, showing significant hardening on the periphery, which was conducive to the formation of PTF mode. However, large longitudinal cracks also existed in the center of the MA-RSW nugget, which may have been the main reason for the IF mode. The microhardness of MP-RSW and MPMA-RSW was similar, showing slight softening in the center and a lack of stratification. The low-hardness sites in MP-RSW coincided with penetrating cracks and central voids (~100 µm in diameter). The small void defects (~20 µm in diameter) in MPMA-RSW shown in Part 1 might have been the cause of the small number of blue low-hardness sites in the nugget center. The hardness results showed that the hardness of MPMA-RSW was not significantly improved compared with other processes. Therefore, the obvious difference concluded from Figs. 8 and 9 is the degree and scale of defects, which may have been the main reason for the change in fracture mode.

Fractography Analysis

The calculation of the 3D shear strength and the energy absorption per unit 3D area has shown that the weld nugget of MPMA-RSW had stronger fracture toughness than those produced by other processes. To further study the toughness of the weld and the micro-defects affecting the fractures, the micro-morphology of the fractures is observed in Fig. 10. The observation regions are marked with Roman numerals I, II, and III in Figs. 6A–D. Region I is located at the center of the fracture surface. In RSW, MA-RSW, and MP-RSW fracture centers, distinct eggcrate features are observed, indicative of solidification cracks, as shown in Figs. 10A1–C1. The eggcrate morphology arises from separating opposing cellular or dendritic fronts along a thin liquid film at the end of solidification (Ref. 25). Fine solidification cracks were observed at the fracture center of MPMA-RSW, and the eggcrate structure was not prominent (in Fig. 10D1), suggesting a certain load-bearing capacity.

Through comprehensive observation of the fracture surfaces, it was found that in each fracture surface, there were regions that were relatively flat overall and had large tear ridges sparsely distributed, indicating insufficient toughness

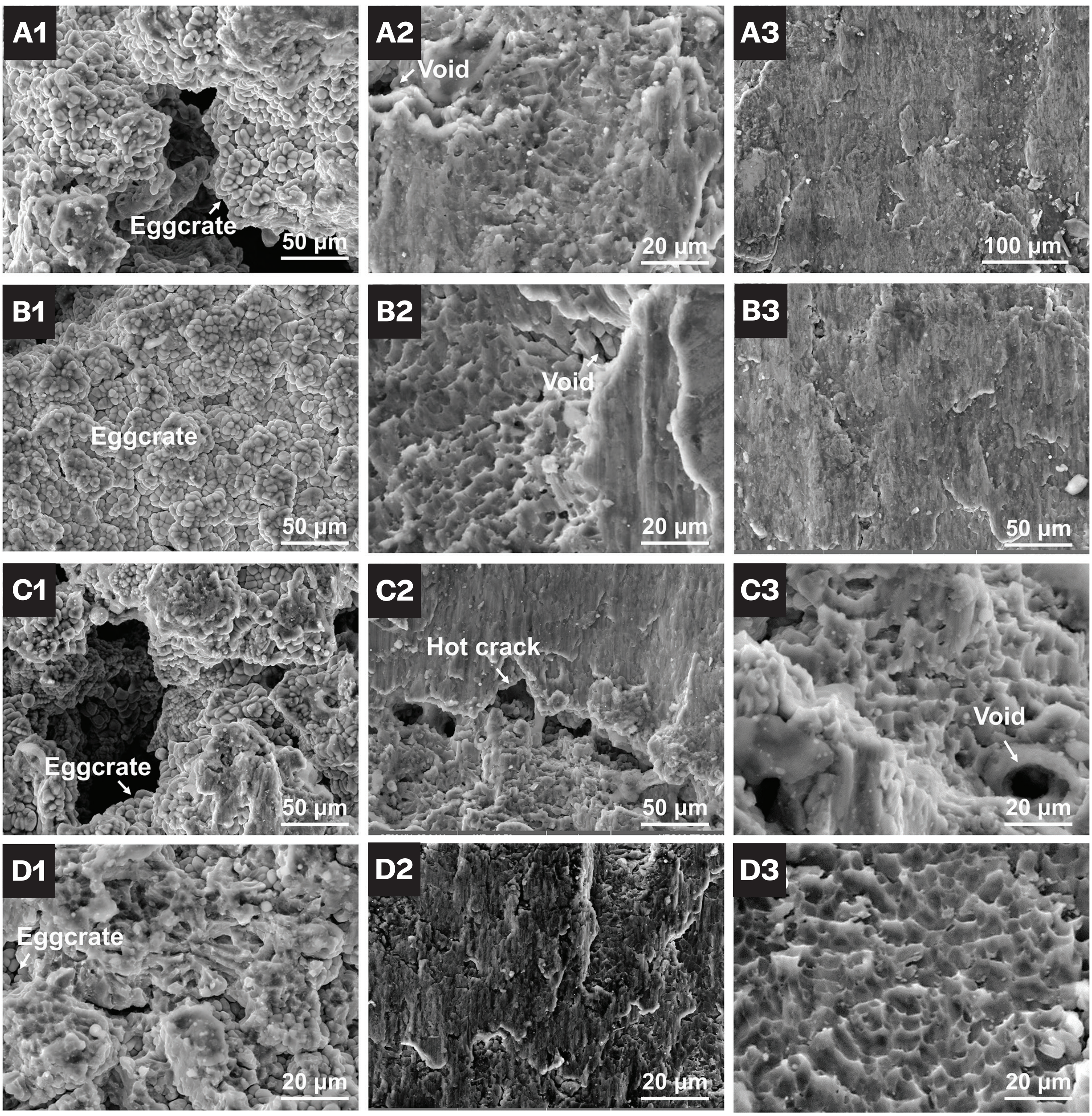

Fig. 10 — Magnified fracture surfaces of: A1–A3 — RSW; B1–B3 — MA-RSW; C1–C3 — MP-RSW; D1–D3 — MPMA-RSW. The regions observed in A1–D1 correspond to the Region I depicted in Figs. 6A–D, and A2–D2 correspond to Region II in Figs. 6A–D, and A3–D3 correspond to Region III in Figs. 6A–D.

of the fracture surface and featuring brittle transgranular fracture (Figs. 10A3, B3, C2, and D2). However, there were also numerous dimples locally (Figs. 10A2, B2, C3, and D3). Therefore, each fracture surface exhibited a mixed ductile-brittle fracture mode. Compared with Figs. 10B2, C3, and D3, the dimple characteristics in Fig. 10A2 are less prominent, and the fracture surface is relatively flat. To comprehensively reflect the characteristics of the fracture surfaces, the areas with typical dimples were marked in Figs. 6A–D. It can be seen that the typical dimple regions in RSW and MA-RSW are fewer and more dispersed. In contrast, the MPMA-RSW and MP-RSW possess more dimple regions, concentrated at the fracture surfaces' rear position. Under the PTF mode, the front part of the fracture surface was subjected to shear force, resulting in a relatively rapid fracture and, thus, a flatter fracture surface. The observation shows that fewer defects were found in the fracture surface of the MPMA-RSW joint, and the MA, MP, and MPMA processes can all improve the fracture toughness of the welds.

Conclusions

This study systematically investigated the effects of multipulse and magnetic-assisted resistance spot welding processes on expulsion suppression, nugget morphology, and fracture behavior in AA7075 welds. The findings are summarized as follows:

1. Using MA increased the tendency to expulsion. The MP parameters effectively suppressed expulsion by controlling nugget growth relative to the corona bond. During the cooling phases, the corona bond expanded dynamically, concurrently preventing nugget breakthroughs and minimizing porosity defects in both MP-RSW and MPMA-RSW welds.

2. Implementing MP and MPMA processes significantly altered crack propagation paths. In traditional RSW and MA-RSW, cracks propagated linearly along the interface, leading to an interfacial failure mode. By contrast, in MP-RSW and MPMA-RSW, cracks deviated from the original path within the nugget, bypassing the center and preferentially extending along the nugget edges, thus forming partial through-thickness failure mode. This transition was attributed to fewer void defects in the MP and MPMA processes, as there was no major evolution in nugget hardness.

3. Shear strengths across the four processes ranked as follows: MPMA-RSW > MP-RSW ≥ MA-RSW > RSW. The fracture centers in RSW, MA-RSW, and MP-RSW displayed distinct eggcrate features, showing signs of solidification cracks. Fractography analysis also confirmed the enhancing effect of the MA, MP, and MPMA processes on the fracture toughness of the solder joints.

These results highlight that the MPMA-RSW process significantly enhances expulsion suppression, weld defect reduction, and fracture toughness improvement in AA7075 welds due to its ability to control thermal cycles and refine microstructure dynamically. This novel approach presents a viable solution for high-performance applications in lightweight automotive structures and aerospace components.

Acknowledgments

The authors would like to acknowledge the financial support of the National Natural Science Foundation of China (Grant Nos. 52025058 and 52205396), the Young Elite Scientists Sponsorship Program by CAST (Grant No. 2022QNRC001), the Shanghai Rising-Star Program (Grant No. 23QB1405700), and the Guangxi Science and Technology Major Program (Grant No. AA23062069).

In addition, the authors would like to acknowledge the financial support of the National Natural Science Foundation of China (Grants 52025058, 52205396), National Defense Basic Scientific Research Program of China (Grant JCKY2021203B074), the Young Elite Scientists Sponsorship Program by CAST (Grant 2022QNRC001), the Shanghai Rising-Star Program (Grant 23QB1405700), and the Guangxi Science and Technology Major Program (Grant AA23062069).

References

1. Zhang, B., Ma, Y., Yu, F., Liu, Y., Zhou, E., Fan, Z., Ge, E., Li, Y., and Lin, Z. 2024. Strengthening flat-die friction self-pierce riveting joints via manipulating stir zone geometry by tailored rivet structures. *International Journal of Machine Tools and Manufacture* 203(12). DOI: 10.1016/j.ijmachtools.2024.104223

2. Qi, L., Zhang, Q., Ma, Y., Xu, Y., Han, X., and Li, Y. 2021. A comparative study on mechanical performance of traditional and magnetically assisted resistance spot welds of A7N01 aluminum alloy. *Journal of Manufacturing Processes* 66: 133–144. DOI: 10.1016/j.jmapro.2021.04.006

3. Li, Z., Teng, Z., Chen, J., Queval, J., Qian, C., Brown, J., Xia, Y., and Li, Y. 2025. Enhancing AA7075 spot welding with multi-pulsed current and magnetic fields: Part 1 - Materials characterization. *Welding Journal* 104(8): 286-s to 297-s. DOI: 10.29391/2025.104.020

4. Chen, R., Lou, M., Li, Y., and Carlson, B. E. 2019. Improving weldability of Al-Si coated press hardened steel using stepped current pulse schedule. *Journal of Manufacturing Processes* 48: 31–43. DOI: 10.1016/j.jmapro.2019.10.010

5. Zhang, H., 1999. Expulsion and its influence on weld quality. *Welding Journal* 78(11): 373-s to 380-s.

6. Senkara, J., Zhang, H., and Hu, S. J. 2004. Expulsion prediction in resistance spot welding. *Welding Journal* 83(4): 123-s to 132-s.

7. Valaee-Tale, M., Sheikhi, M., Mazaheri, Y., Malek Ghaini, F., and Usefifar, G. R. 2020. Criterion for predicting expulsion in resistance spot welding of steel sheets. *Journal of Materials Processing Technology* 275. DOI: 10.1016/j.jmatprotec.2019.116329

8. Ma, C., Bhole, S. D., Chen, D. L., Lee, A., Biro, E., and Boudreau, G. 2006. Expulsion monitoring in spot welded advanced high strength automotive steels. *Science and Technology of Welding and Joining* 11: 480–487. DOI: 10.1179/174329306x120895

9. Farson, D. F., Chen, J. Z., Ely, K., and Frech, T. 2003. Monitoring of expulsion in small scale resistance spot welding. *Science and Technology of Welding and Joining* 8: 431–436. DOI: 10.1179/136217103225009071

10. Xia, Y.-J., Su, Z.-W., Li, Y.-B., Zhou, L., and Shen, Y., 2019. Online quantitative evaluation of expulsion in resistance spot welding. *Journal of Manufacturing Processes* 46: 34–43. DOI: 10.1016/j.jmapro.2019.08.004

11. Xia, Y.-J., Song, Q., Yi, B., Lyu, T., Sun, Z., and Li, Y. 2025. Improving out-of-distribution generalization for online weld expulsion inspection using physics-informed neural networks. *Welding in the World*. DOI: 10.1007/s40194-025-01950-6

12. Lv, T.-L., Xia, Y.-J., Murugan, S. P., Okigami, F., Ghassemi-Armaki, H., Carlson, B. E., and Li, Y., 2025. Multi-physical process simulation

of resistance spot welding available for synthetic data generation. *Journal of Manufacturing Processes* 141: 709–724. DOI: 10.1016/j.jmapro.2025.03.024

13. Li, Z., Huo, Z., Zhao, X., Xia, Y.-J., Huang, S., Liu, H., Xi, X., and Li, Y. 2024. Effect of external magnetic field on microstructures and mechanical properties of Ti-2Al-1.5Mn titanium alloy resistance spot welds. *Journal of Manufacturing Processes* 124: 1273–1284. DOI: 10.1016/j.jmapro.2024.07.010.

14. Wung, P., Walsh, T., Ourchane, A., Stewart, W., and Jie, M. 2001. Failure of spot welds under in-plane static loading. *Experimental Mechanics* 41: 100–106. DOI: 10.1007/BF02323111

15. Chao, Y. J. 2003. Ultimate strength and failure mechanism of resistance spot weld subjected to tensile, shear, or combined tensile/shear loads. *Journal of Engineering Materials and Technology* 125: 125–132. DOI: 10.1115/1.1555648.

16. Pouranvari, M., Asgari, H. R., Mosavizadch, S. M., Marashi, P. H., and Goodarzi, M. 2007. Effect of weld nugget size on overload failure mode of resistance spot welds. *Science and Technology of Welding and Joining* 12: 217–225. DOI: 10.1179/174329307x164409

17. Chen, R., Lou, M., Li, Y., and Carlson, B. E. 2022. A Critical Nugget Size Prediction Model for Al–Si-Coated Press Hardened Steel Resistance Spot Welds. *Journal of Manufacturing Science and Engineering* 144. DOI: 10.1115/1.4051680

18. Pouranvari, M., Marashi, S. P. H., 2011. Failure mode transition in AHSS resistance spot welds. Part I. Controlling factors. *Materials Science and Engineering: A* 528: 8337–8343. DOI: 10.1016/j.msea.2011.08.017

19. Florea, R. S., Solanki, K. N., Bammann, D. J., Baird, J. C., Jordon, J. B., and Castanier, M. P. 2012. Resistance spot welding of 6061-T6 aluminum: Failure loads and deformation. *Materials & Design* 34: 624–630. DOI: 10.1016/j.matdes.2011.05.017

20. Huang, M., Zhang, Q., Qi, L., Deng, L., and Li, Y., 2020. Effect of external magnetic field on resistance spot welding of aluminum alloy AA6061-T6. *Journal of Manufacturing Processes* 50: 456–466. DOI: 10.1016/j.jmapro.2020.01.005

21. Qi, L., Li, Z., Zhang, Q., Wu, W., Huang, N., and Li, Y., 2021. Electromagnetic stirring control for resistance spot welding of SiCp/Al composites. *Journal of Manufacturing Processes* 68: 1271–1279. DOI: 10.1016/j.jmapro.2021.06.048

22. ISO 6892–1, *Metallic materials — tensile testing — Part 1: Method of test at room temperature*. 2019.

23. Shen, Y., Xia, Y.-J., Li, H., Zhou, L., Li, Y.-B., and Pan, H.-T., 2021. A novel expulsion control strategy with abnormal condition adaptability for resistance spot welding. *Journal of Manufacturing Science and Engineering* 143. DOI: 10.1115/1.4051011

24. Hu, S., Haselhuhn, A. S., Ma, Y., Li, Y., Carlson, B. E., and Lin, Z. 2021. Sensitivity of dissimilar aluminum to steel resistance spot welds to weld gun deflection. *Journal of Manufacturing Processes* 68: 534–545. DOI: 10.1016/j.jmapro.2021.05.059

25. Lippold, J. C. 2014. *Welding metallurgy and weldability*. John Wiley & Sons.

ZHUORAN LI, **CHANGMING QIAN**, **JORDAN QUEVAL**, **YUJUN XIA** (*xyjdbgt6509@sjtu.edu.cn*), and **YONGBING LI** are with Shanghai Key Laboratory of Digital Manufacture for Thin-walled Structures, State Key Laboratory of Mechanical System and Vibration, School of Mechanical Engineering, Shanghai Jiao Tong University, Shanghai, China. **ZHENKE TENG** and **JASON BROWN** are with Global Manufacturing Engineering, General Motors Global Technical Center, Warren, Mich. **RUIMING CHEN** is with Shanghai Smart Fusion Industrial Equipment Co. Ltd., Shanghai, China.